Performance of large area CsI-RICH prototypes for ALICE at LHC

for the ALICE collaboration

A. Di Mauro[a,*], D. Cozza[b], M. Davenport[a], D. Di Bari[b], D. Elia[b], P. Martinengo[a], A. Morsch[a], E. Nappi[a,b], G. Paić[a,c], F. Piuz[a], S. Stucchi[a], G. Tomasicchio[b], T.D. Williams[a]

[a]CERN, European Organization for Nuclear Research, 1211 Geneva, Switzerland
[b]INFN and Dipartimento Interateneo di Fisica dell'Universitá di Bari, Bari, Italy
[c]Ohio State University, Columbus, OH, USA

Abstract

We present the performances of large area CsI-RICH prototypes obtained in single-particle events. The differential quantum efficiency of the photocathodes has been deduced from Cherenkov rings by means of two different procedures: a direct measurement with a thin NaF radiator and a Monte Carlo-based estimation for a C_6F_{14} radiator. A factor of merit of 45 cm^{-1} has been found for the typical detector configuration. Two angle reconstruction algorithms have been used and the different errors affecting the Cherenkov angle resolution have been estimated combining the analytical treatment and the Monte Carlo simulation. Also the dependence on radiator thickness, Cherenkov ring radius, chamber voltage and particle incidence angle has been studied. © 1999 Elsevier Science B.V. All rights reserved.

1. Introduction

In the framework of the development of a large area CsI-RICH detector for ALICE (A Large Ion Collider Experiment [1]) at LHC, various prototypes, having active areas up to ~ 1 m^2, have been studied in beam tests aiming at the evaluation of two fundamental properties: the CsI photocathode (PC) quantum efficiency (QE) and the Cherenkov angle resolution [2].

The differential QE of CsI PC's is usually measured in laboratory with dedicated UV-setups;

however, these can be operated generally only with small size samples. In the present work we demonstrate how the QE dependence on wavelength of a large-area CsI PC can be evaluated from the measurement of the Cherenkov light in a RICH detector.

In the last part of the paper, to characterize the performance in terms of particle identification capability, the main results of a detailed examination of the angular resolution will be discussed.

2. Experimental setup

The detector configuration is schematically shown in Fig. 1, while a complete description of the
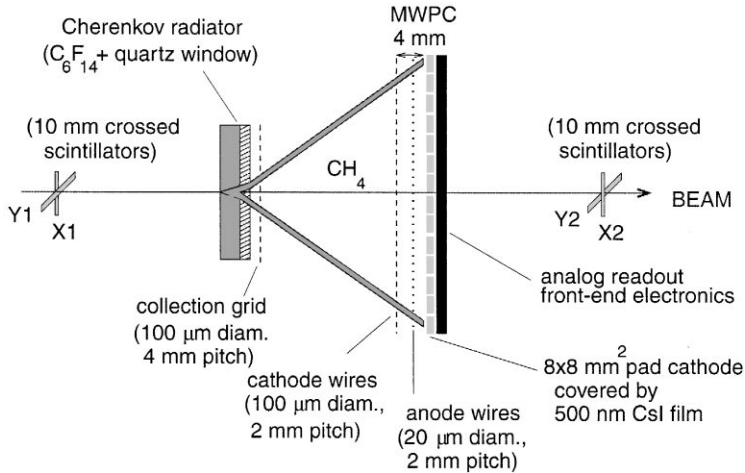
---

* Corresponding author.

Fig. 1. Scheme of the CsI-RICH prototype geometry.

test-beam setup can be found in Ref. [2]. The RICH detector has a proximity focusing geometry with a multiwire chamber having a CsI photocathode segmented into $8 \times 8 \, mm^2$ pads, with a 2-d analog multiplexed readout.

Tests of a prototype of $32 \times 30 \, cm^2$ active area (proto-1) have been performed in the CERN PS/T11 test-beam composed of protons and pions in the 1–3.5 GeV/c momentum range. Two crossed plastic scintillator doublets, 2 m apart, define the trigger geometry covering an area of $1 \, cm^2$ of the detector, with a beam divergence $\leq 1 \, mrad$. A time-of-flight system based on two scintillators, 10 m apart, provides offline discrimination between protons and pions. Proto-1 can be equipped with a NaF radiator or an adjustable thickness C_6F_{14} liquid radiator with a 3 mm quartz window.

A larger prototype composed of 4 PC's of $64 \times 40 \, cm^2$ (proto-2), for a total size of $\sim 1.3 \times 0.8 \, m^2$, has been tested at the CERN SPS/H4 350 GeV/c pions test-beam. In this case the two crossed scintillator doublets defining the beam are about 10 m apart, while the radiator tray has a fixed thickness of 10 mm with a 5 mm quartz window.

3. Event analysis

Depending on detector configuration, beam momentum and particle hit point, a Cherenkov fiducial zone is located in the pad plane: it is an annular region where all the Cherenkov photons may be detected. For QE evaluation purposes it is important to establish such a fiducial zone, since the radiation spectrum is well defined inside it.

A fundamental step of the event processing is the cluster deconvolution: it is expected that a certain fraction of single photoelectron clusters may overlap originating larger clusters with multiple local pulse-height (PH) maxima. A contribution from secondary processes is also expected; however due to the small anode–cathode gap (2 mm) and the pad size (8 mm), feedback photons are mostly contributing to the same cluster created by the primary avalanche.

Clusters are first counted as *raw* clusters and after image processing as *resolved* clusters. Raw clusters are classified into three categories depending on the size and the PH distribution (Fig. 2):

- *Class* 1: clusters of one, two or three pads (row or L-shaped) when the PH maximum is in the central pad, assumed to correspond to single photoelectrons;
- *Class* 2: clusters of three pads when the PH maximum is not in the central pad, assumed to correspond to two photoelectrons;
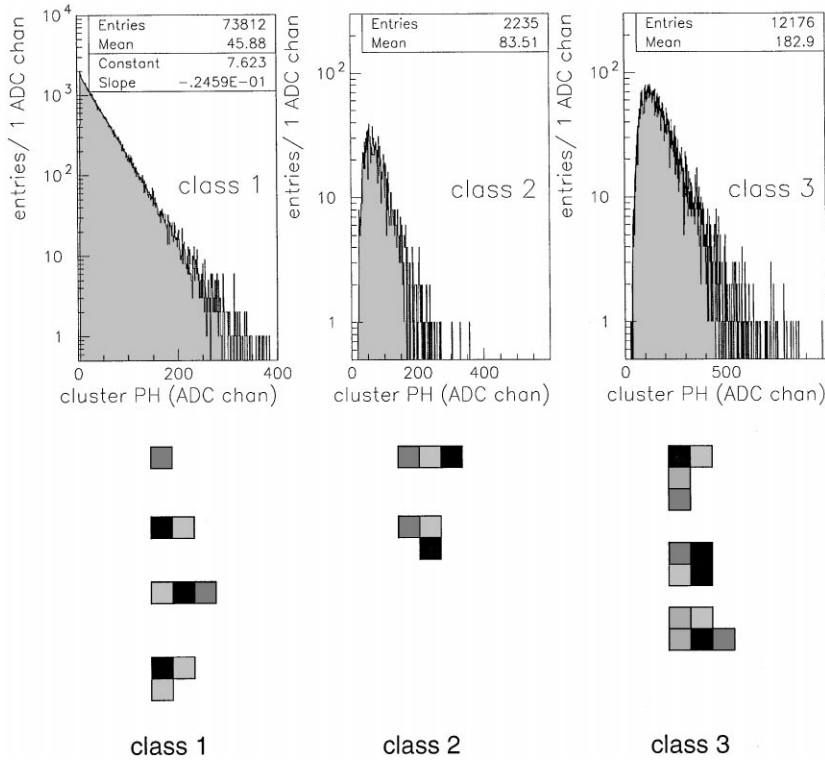- *Class* 3: clusters of more than three pads, assumed to correspond to two or more photoelectrons.

Fig. 2. (top) The total PH distributions of the three classes of *raw* clusters and (bottom) the geometrical features for each class (the darker the grey tone, the larger the pad PH).

Fig. 2 also presents the cluster PH distribution for each class, from test-beam events with proto-2 operated with CH_4 at 2100 V. In these conditions the class 1 PH distribution is generally exponential and the single-electron mean PH A_0, namely the chamber gain, can be deduced from the slope of the fit (also reported in the figure). The average and the shape of the PH distributions relative to class 2 and 3 clusters, compared to that of class 1, indicate clearly the contribution of two or more photoelectrons.

In the majority of the cases class 2 and 3 clusters can be *resolved* into smaller sized clusters by an algorithm producing n resolved clusters when n local PH maxima are found in the original raw cluster.

Finally, the impact position of particles and photons, for clusters of more than one pad, is evaluated with the centroid finding method, while for single-pad clusters it is assumed to be in the pad centre.

4. CsI QE evaluation in Cherenkov events

The knowledge of the spectrum of the Cherenkov radiation and the transmission of the media traversed by the photons has been exploited to evaluate the differential QE of large area CsI PCs with two different approaches. The first allows a direct measurement of the CsI QE curve making use of the large dispersion of the refractive index of a NaF radiator [3]. The other is based on the simulation of Cherenkov events aiming at the *tuning* of the quantum response through the reproduction of main quantities evaluated in beam tests.

4.1. Direct measurement with a NaF radiator

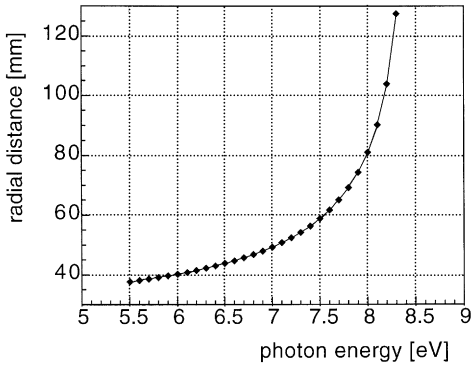The number of photons having an energy within E, $E + dE$, reaching the photocathode, can

Fig. 3. Cherenkov photons distance from the ring centre as a function of photon energy, calculated for 2 GeV/c protons, 2 mm NaF radiator and 28 mm proximity gap.
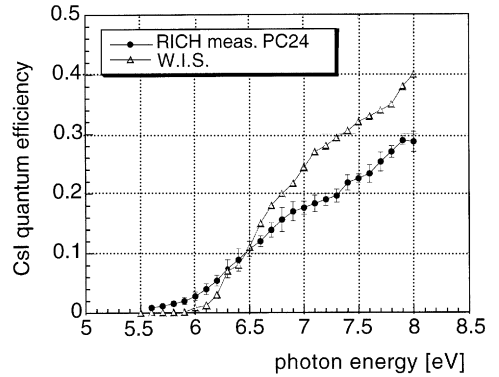

Fig. 4. PC24 QE, deduced from the analysis of Cherenkov rings generated in a NaF radiator, and the CsI QE obtained at the W.I.S. from photocurrent measurement on a small sample evaporated on stainless steel substrate.

be calculated as

$$N_{\text{phot}}(E) = 370 \, T_r \int_E^{E+dE} \sin^2\theta_c(E) \prod_i T_i(E) \, dE \qquad (1)$$

where T_r is the radiator thickness, θ_c is the Cherenkov angle and T_i is the transmission of the ith traversed medium. In the setup used, the upper limit of the spectral acceptance is set by the collection electrode frame (Fig. 1) which absorbs Cherenkov photons of energy above a value depending on the particle momentum (8 eV in the case of 2 GeV/c protons); the lower limit is set by the CsI photoelectric threshold. Because of the large NaF chromaticity the Cherenkov fiducial zone can be subdivided into circular areas such that when a photon is counted in the nth zone its energy falls in a bin of width ΔE centred at E_n. Fig. 3 shows the dependence of the radial distance of the photon impact from the particle impact point as a function of the emitted photon energy. The values were calculated for photons produced by 2 GeV/c protons, a proximity gap of 28 mm and an emission point in the middle of a 2 mm NaF radiator.

Assuming that all the quantities depending on energy are constant in each interval of width $\Delta E = 0.1$ eV, the QE can be calculated with the approximated relation

$$QE(E_i) = \frac{N_{\text{phel}}(E_i)}{370 T_r \sin^2\theta_c(E_i) \prod_j T_j(E_i) \Delta E \varepsilon_{\text{det}}} \qquad (2)$$

where $N_{\text{phel}}(E_i)$ is the number of photoelectrons counted in the ith interval and ε_{det} is the single-

electron detection efficiency. The accuracy of this method is limited by the proximity focusing error, resulting in the contamination, in a given energy bin, of photons belonging to adjacent energy bins. To minimize this effect a radiator as thin as possible has to be used, allowing narrower energy bins to be defined. We present the results obtained using proto-1 equipped with PC24 and a NaF radiator 2 mm thick. Several runs have been taken in different combinations of proton beam momenta (2 and 3 GeV/c) and proximity gaps (24.5, 28, 33, 43 and 48 mm). The average QE curve of these measurements is reported in Fig. 4 and, for comparison, the CsI QE of a small sample, evaporated on stainless steel substrate, measured at the Weizmann Institute of Science (W.I.S.) by Breskin et al. [4,5].

At energies below the CsI photoelectric threshold (~ 6 eV) a negligible QE is expected. The large values measured, shown in Fig. 4, could be attributed to the feedback photons originated by the minimum ionizing particle (MIP). Indeed these energy bins correspond to small radial distances from the MIP impact (Fig. 3). This interpretation is supported by the results obtained using the Monte Carlo simulation described in the next paragraph.

4.2. Evaluation with Monte Carlo simulation of C_6F_{14} events

In the original Monte Carlo simulation program RICHSIM all physical processes, from the

Cherenkov emission to the signal induction on the photocathode pad plane, are taken into account. Several input parameters can be specified, in order to match the experimental conditions: type of Cherenkov radiator (NaF or C_6F_{14}), its thickness T_r and UV-transmission in the 160–220 nm range, proximity gap width T_g, O_2 and H_2O contamination (in ppm), CsI QE curve, detector rotation angles, mean pedestal and sigma for electronic noise, chamber gain, photon feedback rate. Only the most peculiar sections of the simulation will be described here.

4.2.1. Cherenkov photon generation: the C_6F_{14} refractive index

The number of photons generated along the particle trajectory in the radiator is drawn from a Poisson distribution with mean N_{av} given by the integral of the Frank–Tamm relation over the energy range of detector response. The emission point in the radiator is uniformly distributed while the Cherenkov photon energy is sampled from a density function

$$f(E) = 1 - \frac{1}{n^2(E)\beta^2}. \qquad (3)$$

Then the Cherenkov angle is calculated from the radiator refractive index. For C_6F_{14}, before the recent measurements done by Fokitis et al. from DELPHI [6], only Séguinot's data [7] were available in the far UV. The linear extrapolation, $n(E) = a + b \cdot E$, of Séguinot's values to the range of interest (with $a = 1.2177$, $b = 0.00928$ eV^{-1}) results in a bad fit of experimental data; on the contrary, they are well reproduced using in *RICHSIM* $a = 1.177$, $b = 0.0172$ eV^{-1}, a parametrization in rather good agreement with DELPHI measurements (Fig. 5).

It should be noticed that the C_6F_{14} sample purity and temperature (coefficient $dn/dT = -5 \times 10^{-4}$ $^\circ$C^{-1} given by the supplier) may play an important role in explaining discrepancies among different measurements.

4.2.2. Photon propagation and photoconversion at the CsI photocathode

Each Cherenkov photon is propagated through the detector, undergoing absorption and interactions at the media boundaries (Fig. 6).
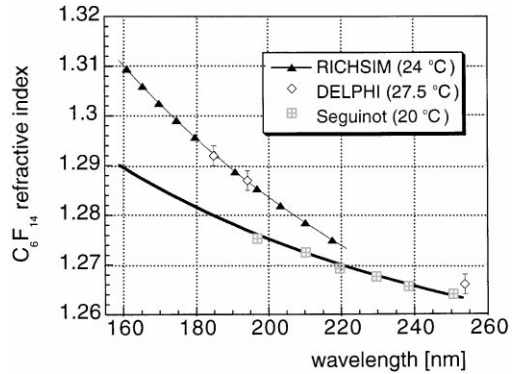

Fig. 5. The C_6F_{14} refractive index (DELPHI values by courtesy of E. Fokitis, S. Maltezos and P.G. Moyssides).
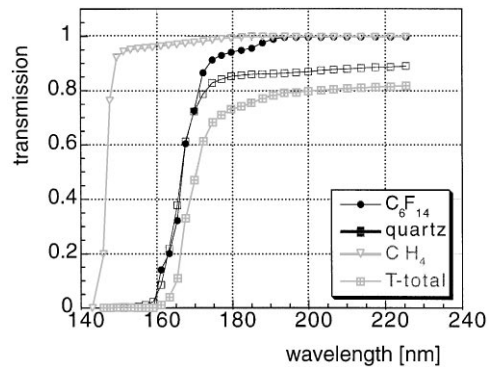

Fig. 6. Cherenkov photons transmission in detector media, calculated for $\beta = 1$ particles, emission point at about half of the 10 mm C_6F_{14} radiator, 5 mm quartz window (Heraeus) and 103 mm proximity gap. The total T curve includes also the reflection losses at radiator/quartz interface, quartz/gas interface and electrodes.

At the point of photoconversion, Fresnel reflection losses on the CsI PC surface are taken into account to make the PC response varying with the photons incidence angle θ_o. The Fresnel reflection probablity is calculated using a complex refractive index for CsI [8]; then the following correction factor S_r for surface roughness is included [9]:

$$S_r = \exp^{-4\pi\cos\theta_o\sigma_r/\lambda} \qquad (4)$$

where λ is the photon wavelength and σ_r is the surface roughness parameter (which is ~ 20 nm in our case [2]).
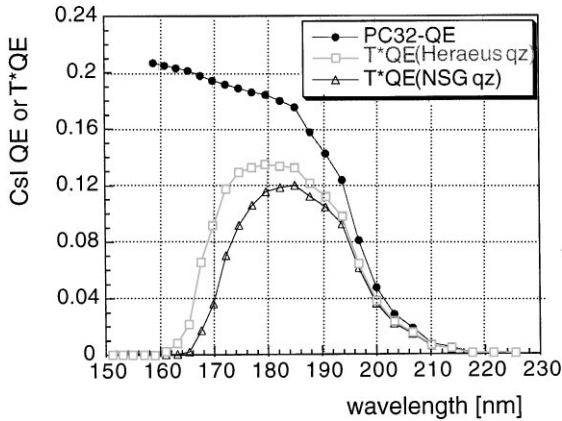
Fig. 7. PC32 QE evaluated from simulation and the convolution with the total transmission, defining the detected photon spectrum, obtained with two different quartz windows.
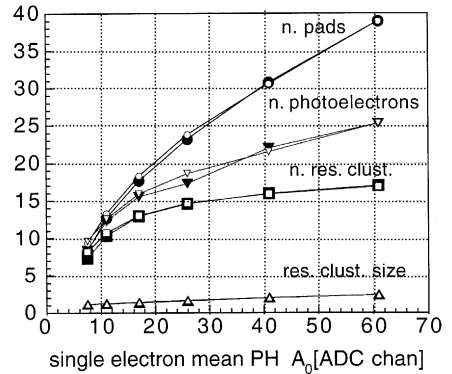

Fig. 8. Variation of main quantities of the Cherenkov ring analysis (number of pads/event, number of resolved clusters/event, resolved cluster size and number of photoelectrons/event) as a function of single electron mean PH A_0 in proto-2, PC32, 350 GeV/$c\pi$ SPS test-beam (1 ADC channel corresponds to 0.17 fC). Full symbols: measurements; empty symbols: simulation.

The PC32 QE used to reproduce test-beam data is shown in Fig. 7 together with the convolution with the total transmission curves obtained with two quartz windows of different quality, supplied by Heraeus and NSG.

4.2.3. Generation of signal on pads and photon feedback

The single-electron avalanche charge is drawn from an exponential distribution due to the CH_4 and the moderate gain ($\leq 10^5$) in use. Then a number N_{pf} of feedback photons is iteratively generated proportionally to the total avalanche charge $Q_t : N_{pf} = K_{pf} Q_t$; K_{pf} is the measured CH_4 feedback rate [10] corrected for the so-called *visible gain*: the measured charge is smaller than Q_t due to both the signal sharing among electrode elements and the front-end electronics peaking time. The secondary photons are generated with an isotropic angular distribution from the avalanche position on the sense wire, sampling the three C emission lines: 156 (30%), 166 (57%) and 193 nm (13%) [11]. Incorporating the reflection at anode wires and at the CsI PC surface (including roughness) proved to be necessary for a correct simulation.

Finally, the electrostatic model used for the signal induction is based on the single-parameter Gatti formula [12,13].

4.2.4. Electronic noise contribution and PH thresholding

The electronic noise is generated on each pad with a Gaussian distribution having a standard deviation determined experimentally. Then a PH thresholding with pedestal subtraction produces the event that can be analysed by means of the same test-beam analysis software.

4.2.5. Analysis results for chamber gain scan

In Fig. 8 are reported the main multiplicities, measured and simulated, as a function of the single electron mean PH A_0, namely the chamber gain, given in ADC channels (1 ADC channel corresponds to 0.17 fC, i.e. ~ 1060 e$^-$). The measured number of photoelectrons is calculated as ratio between the total PH and A_0 while the simulation value is the *true* number of detected photoelectrons in *RICHSIM* events. The saturation in the resolved clusters multiplicity is due to the detection efficiency plateau while the continuous increase of the number of pad hits is related to the larger induced signal as well as to the increasing feedback photolectrons multiplicity. This interpretation is well supported by the plot in Fig. 9 showing the single contributions to the detected photoelectrons.

As a concluding remark, the simulation allowed to estimate the factor of merit $N_0 = 45$ cm^{-1} with
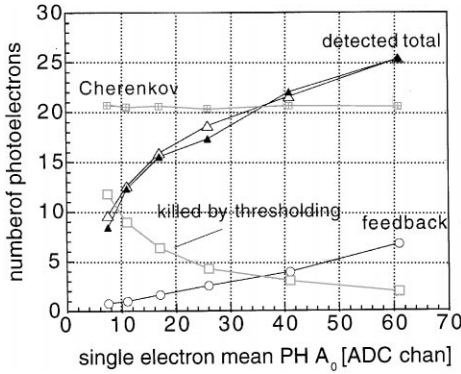
Fig. 9. The number of photoelectrons as a function of single electron mean PH A_0 from beam test data is compared to the same quantity obtained from the simulation (1 ADC channel corresponds 0.17 fC). The single contributions to the total number of photoelectrons, estimated by simulation, are also reported: detected total = Cherenkov + feedback − killed by thresholding.

proto-2/PC32 in typical operation conditions (chamber gain $A_0 = 41$ ADC channels, single-electron detection efficiency $\varepsilon_{\text{det}} = 90\%$).

5. Cherenkov angle resolution

We have carried out an investigation of all the aspects influencing the spread of the reconstructed angle distribution, based on a combined analysis of beam test and Monte Carlo events as well as on the analytical estimation of single contributions: chromatic, geometric, localization and particle incidence angle [14].

The angle reconstruction procedure defines a relation $\theta_c = \theta_c(E, T_r, R, \theta_p)$ from which the angular resolution, referring to the adopted algorithm, can be analytically estimated as

$$\sigma_{\theta_c} = \left[\sum_{i=1}^{4} \left(\frac{\partial \theta_c}{\partial v_i} \sigma_{v_i} \right)^2 \right]^{1/2} \tag{5}$$

where θ_c is the Cherenkov angle, the variables v_i: E, T_r, R, θ_p are the photon energy, the radiator thickness, the ring radius and the particle incidence angle, respectively, while σ_{v_i} are the corresponding r.m.s. errors.

Two methods have been used for the Cherenkov angle reconstruction, in real and simulated events

[14]. Since the photon *emission point* in the radiator, X_{ep} and the photon energy are unknown, in both methods, the angle reconstruction is achieved by fixing them at the most probable values. In particular, X_{ep} is about 5.2 mm for perpendicular tracks in a 10 mm radiator; it differs from $T_r/2$ since photons generated in the first radiator half have a larger probability of being absorbed due to their longer path in the C_6F_{14}. The average energy E_{av} is 6.85 eV over the detector response (Fig. 7).

The first procedure, called *β-method*, is a direct transformation of the measured ring radius R into a θ_c value through a relation which can be established in case of perpendicular incidence and known β. Fixing the photon emission point and energy to the respective average values, the radiator and the quartz window contributions to R, ΔR_{rad} and ΔR_{qz}, become constant terms and one can easily get R_o from $R = \Delta R_{\text{rad}} + \Delta R_{\text{qz}} + R_o$. In turn $R_o = T_g \tan \theta_o$ where T_g is the proximity gap thickness and θ_o is the Cherenkov angle in the proximity gap. Then, using Snell's law and Cherenkov's relation to eliminate the dependence on the refractive index, θ_c can be reconstructed as

$$\theta_c = a \cos \left(\frac{1}{\sqrt{\beta^2/(1 + (T_g^2/R_o^2)) + 1}} \right). \tag{6}$$

The second algorithm, the *loop-method*, is based on the search of the best angle through an iteration procedure described in Ref. [15].

Fig. 10 shows the reconstructed Cherenkov angle distributions relative to the two methods. A ring resolution of 1.9 mrad has been obtained with the β-method, which, in principle, could be applied also to events where the particle track is not perpendicular (a simple detector rotation is needed), and when $β$ is not known (depending on the application, one has usually three mass hypothesis).

5.1. Contributions to the Cherenkov angle resolution

For the analytical treatment, after having obtained the partial derivatives $(\partial \theta_c / \partial v_i)$ following Ypsilantis' formulation [16], the evaluation of the r.m.s. errors σ_{v_i}, strictly related to the detector response, is needed.
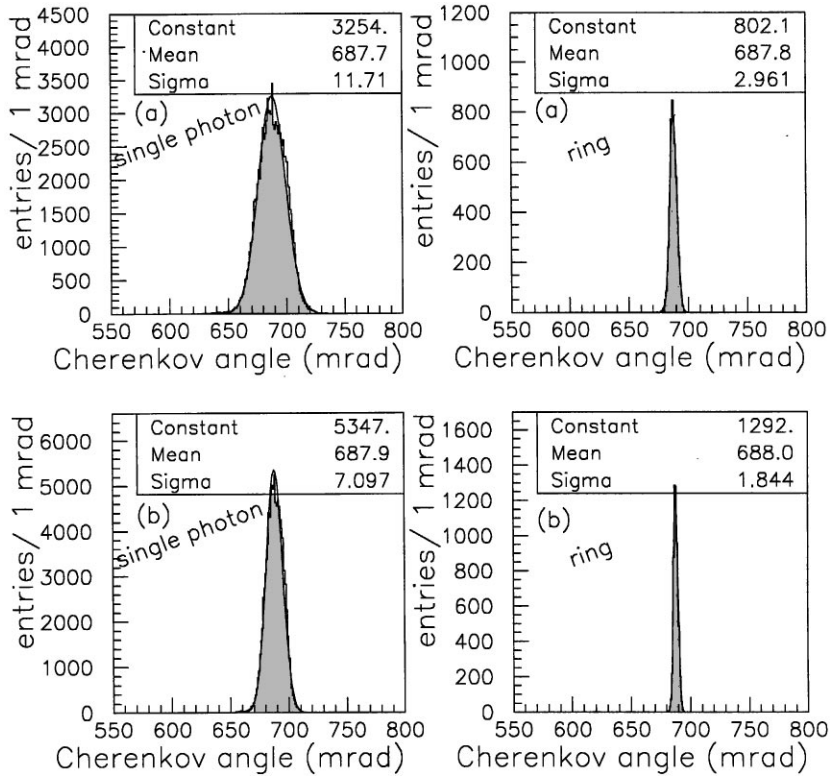
Fig. 10. Single-photon and ring-averaged, Cherenkov angle distributions, from (a) the loop and (b) the β-methods; SPS test-beam, 350 GeV/c π, PC32, single electron mean PH $A_0 = 41$ ADC channels (1 ADC channel corresponds to 0.17 fC).

The chromatic r.m.s. error is $\sigma_E = (dn/dE)\sigma_E^{\text{det}}$, with $dn/dE = 0.0172$ eV^{-1} and $\sigma_E^{\text{det}} = 1.75/\sqrt{24}$ eV (according to the detected photon spectrum reported in Fig. 7 for a Heraeus quartz window). For the geometric r.m.s. error σ_{T_r} the calculation is straightforward: $\sigma_{T_r} = T_r/(\sqrt{12}\cos\theta_p)$. Finally, the total localization r.m.s. error σ_R includes the uncertainty of both particle and photon x, y coordinates: $\sigma_R = 3$ mm. Such a large value, evaluated through *RICHSIM*, results from the poor localization accuracy achievable in single pad clusters ($\sim$ pad size/$\sqrt{12}$) as well as from the photon feedback contribution.

The results of the analytical estimation of each contribution in the two methods are reported in Table 1; for comparison, the same errors have been evaluated with *RICHSIM*, resulting in good agreement with the calculations.

5.2. Optimization of the angular resolution in beam tests

Different tests have been carried out to examine the angular resolution dependence on the Cherenkov ring radius, the chamber gain, the radiator thickness and the particle incidence angle θ_p.

The single errors, $(\partial\theta_c/\partial v_i)\sigma_{v_i}$, and the single-photon angular resolution, σ_{θ_c} are reported in Table 2, from analytical calculation, simulation and measurements, for the *β-method*, at several ring radii. In Table 3 the same quantities, evaluated with the *loop method*, are shown. The σ_{θ_c} simulation values come from the reproduction of test-beam runs, thus including effects related to the detector operating conditions specific to each run, while the calculated values refer to a constant configuration. Besides the good agreement among the different data sets one can notice that the deterioration at

Table 1

Single-photon Cherenkov angle errors from analytical treatment and simulation ($\beta = 1$, $T_r = 10$ mm, $T_g = 103$ mm)

Error	Calculation		Simulation	
	β-method (mrad)	*Loop-method* (mrad)	*β-method* (mrad)	*Loop-method* (mrad)
Chromatic	5.7	9.4	5.9	9.7
Geometric	2.5	4.1	2.6	4.2
Localization	3.1	4.8	3.1	5

Table 2

Single-photon extracted Cherenkov angle errors from analytical treatment, simulation and measurements, in the *β-method*, at several ring radii

Ring radius (mm)	Calculation				Simulation	Measurement
	Chromatic (mrad)	Geometric (mrad)	Localization (mrad)	σ_{θ_c} (mrad)	σ_{θ_c} (mrad)	σ_{θ_c} (mrad)
85	5.76	4.83	5.95	9.7	10.8	11.2
104	5.73	3.78	4.66	8.4	8.2	8.6
122	5.71	3.26	4.01	7.8	7.3	7.5
133	5.7	2.9	3.6	7.43	7.4	7.6
155	5.69	2.53	3.12	7.1	6.8	6.9

Table 3

Single-photon extracted Cherenkov angle errors from analytical treatment, simulation and measurement, in the *loop method*, at several ring radii

Ring radius (mm)	Calculation				Simulation	Measurement
	Chromatic (mrad)	Geometric (mrad)	Localization (mrad)	σ_{θ_c} (mrad)	σ_{θ_c} (mrad)	σ_{θ_c} (mrad)
85	9.4	7.9	9.1	15.9	15.6	16.2
104	9.4	6.2	7.1	13.8	13.3	13.8
122	9.4	5.4	6.1	12.8	12.2	12.4
133	9.4	4.8	5.4	12.2	12	12.4
155	9.4	4.2	4.8	11.6	11.1	11.2

$R < 110$ mm is mainly due to the dominance of the chromatic error. Such contribution could be reduced by the use of a quartz window having a larger wavelength cut-off. Fig. 7 presents the detected photons spectrum, obtained with Heraeus and NSG quartz windows. In the latter case, a $\sigma_E^{det} = 1.4/\sqrt{24}$ eV can be estimated, decreasing the chromatic error by 20% with respect to that

evaluated with the first quartz window. The drop in the number of photons can be compensated by a thicker Cherenkov radiator, with a small degradation of the resolution caused by the larger geometric error. Indeed the resolution evaluated by *RICHSIM* using the worse quartz transmission and 12.5 mm radiator is equal to the best values relative to the higher quality quartz and 10 mm
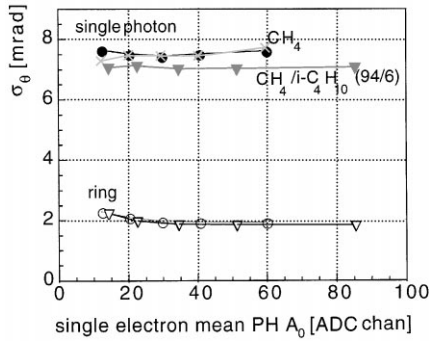
Fig. 11. Angular resolution as a function of the single-electron PH A_0 at $R = 122$ mm, in two gas mixtures; circles and triangles: measurements; crosses: simulation; SPS test-beam, 350 GeV/c π, PC32 (1 ADC channel corresponds to 0.17 fC).
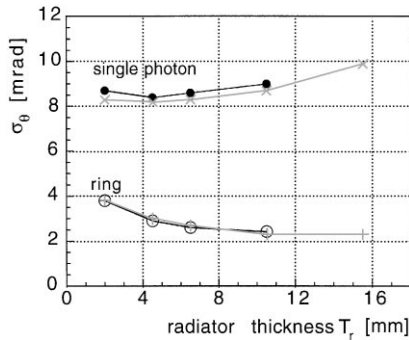

Fig. 12. Angular resolution as a function of radiator thickness at $R = 104$ mm; circles: measurements; crosses: simulation; PS test-beam, 3 GeV/c π, PC24.
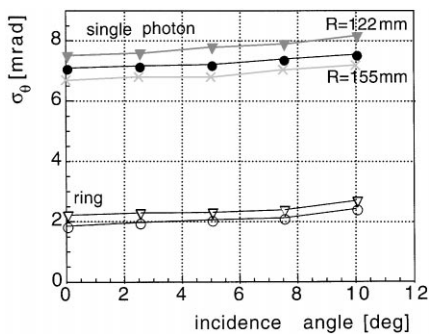

Fig. 13. Angular resolution as a function of the particle incidence angle at a single-electron mean PH $A_0 = 41$ ADC channels (1 ADC channel corresponds to 0.17 fC); circles ($R = 155$ mm) and triangles ($R = 122$ mm): measurements; crosses: ($R = 155$ mm) simulation; SPS test-beam, 350 GeV/c π. The values for the ring radius $R = 122$ mm are relative to PC30 and a proximity gap $T_g = 80$ mm, while those for $R = 155$ mm are relative to PC32 and a proximity gap $T_g = 103$ mm.

C_6F_{14} (single photon: 7 mrad; ring: 1.9 mrad). As a consequence low-cost windows may be used, provided that the performance of the CsI PC could be kept at the standard level.

In Fig. 11 are reported the β-method single-photon angular resolution σ_{θ_c} and ring angular resolution $\sigma_{\theta_c}^{ring}$, from measurements and simulation, as a function of the single-electron mean PH A_0, in two gas mixtures. The stability of σ_{θ_c} with the increase of A_0, at the considered ring radius, could be the result of two opposite effects: the larger feedback contribution, deteriorating the resolution, and the smaller fraction of single pad clusters, improving the resolution. In the mixture with i-C_4H_{10} the single-photon resolution is slightly better than in pure CH_4 probably due to the lower UV-transmission of i-C_4H_{10}, that was not circulated through any filter, reducing the chromatic error and the feedback contribution; however, the ring-averaged resolution is similar to that in pure CH_4 because of the smaller number of Cherenkov photons.

Fig. 12 shows the β-method single-photon and ring-angular resolutions, from measurements and simulation, as a function of the radiator thickness T_r. The small variations of σ_{θ_c} are related to the changes of ring radius and radiator transmission with T_r, while $\sigma_{\theta_c}^{ring}$ increases, as expected, at smaller T_r as a consequence of the reduction of the number of emitted Cherenkov photons.

Finally, in Fig. 13 are reported the β-method single-photon and ring-angular resolutions, from measurements and simulation, as a function of the particle incidence angle θ_p. No significant deterioration of the resolution is observed up to 10º.

6. Conclusions

The described experimental procedures allowed us to estimate a fundamental detector parameter, the QE curve of large-area CsI PCs. The observed discrepancy with the values measured at the W.I.S. may result from the differences in the size of the samples, the nature of the PC substrates and the measurement procedures.

Other quantities, like the C_6F_{14} refractive index, the feedback photon rate and the different contributions to the Cherenkov angle resolution have

been evaluated by means of the Monte Carlo program *RICHSIM*, demonstrating full understanding of the detector behaviour.

Acknowledgements

References

[1] ALICE Collaboration, Technical Proposal, CERN/LHCC 95-71.

[2] ALICE Collaboration, Technical Design Report of The High Momentum Particle Identification Detector, CERN/LHCC 98-19.

[3] M. Hempstead et al., Nucl. Instr. and Meth. A 306 (1991) 207.

[4] A. Breskin et al., Nucl. Instr. and Meth. A 367 (1995) 326.

[5] A. Breskin, Nucl. Instr. and Meth. A 371 (1996) 116.

[6] E. Fokitis, S. Maltezos, P.G. Moyssides, Measurements of the refractive index of DELPHI RICH radiators in liquid phase down to 185 nm, in preparation.

[7] J. Séguinot, Les compteurs Cherenkov: applications et limites pour l'identification des particules. Developpements et perspectives. Ecole J. Curie de Physique Nucleaire, Mabuisson, France, September 1988.

[8] K.I. Said et al., J. Phys. C 10 (1977) 479.

[9] B.J. Stagg, T.T. Charalampopoulos, Appl. Opt. 30 (1991) 4113.

[10] R. Arnold et al., Nucl. Inst. and Meth. A 314 (1992) 465.

[11] H.D. Morgan et al., J. Chem. Phys. 60 (1974) 4734.

[12] E. Mathieson et al., Nucl. Instr. and Meth. A 227 (1984) 277.

[13] E. Mathieson et al., Nucl. Instr. and Meth. A 270 (1988) 602.

[14] A. Di Mauro, Internal Note ALICE 98-34.

[15] R. Arnold et al., Nucl. Instr. and Meth. A 270 (1988) 289.

[16] T. Ypsilantis, J. Séguinot, Nucl. Instr. and Meth. A 343 (1994) 30.